www.czasopisma.pan.pl PAN POLSKA AKADEMIA NAUK www.journals.pan.pl

Arch. Metall. Mater., Vol. 61 (2016), No 2B, p. 1241–1247

DOI: 10.1515/amm-2016-0205

K. WIECZERZAK*#, P. BALA*,**, R. DZIURKA*, M. STEPIEN**, T. TOKARSKI**, G. CIOS**, K. GORECKI*

EXPERIMENTAL AND THERMODYNAMIC STUDY OF SELECTED IN-SITU COMPOSITES FROM THE Fe-Cr-Ni-Mo-C SYSTEM

The aim of the study was to synthesize and characterize the selected in-situ composites from the Fe-Cr-Ni-Mo-C system, additionally strengthened by intermetallic compounds. The project of the alloys was supported by thermodynamic simulations using Calculation of Phase Diagram approach via Thermo-Calc. Selected alloys were synthesized in an arc furnace in a high purity argon atmosphere using a suction casting unit. The studies involved a range of experimental techniques to characterize the alloys in the as-cast state, including optical emission spectrometry, light microscopy, scanning electron microscopy, electron microprobe analysis, X-ray diffraction and microhardness tests. These experimental studies were compared with the Thermo-Calc data and high resolution dilatometry. The results of investigations presented in this paper showed that there is a possibility to introduce intermetallic compounds, such as χ and σ, through modification of the chemical composition of the alloy with respect to Ni_{eq} and Cr_{eq}. It was found that the place of intermetallic compounds precipitation strongly depends on matrix nature. Results presented in this paper may be successfully used to build a systematic knowledge about the group of alloys with a high volume fraction of complex carbides, and high physicochemical properties, additionally strengthened by intermetallic compounds.

Keywords: Fe-Cr-Ni-Mo-C, in-situ composites, intermetallic compounds, dilatometry, microstructure

1. Introduction

Particulate metal matrix composites strengthened by hard phases, such as carbides, are a group of materials characterized by a combination of properties typical for metals (ductility and toughness) and for ceramics (high strengths and moduli). Such a combination of different material groups' advantages leads to an improvement of shear and compressive strengths, and enables maintaining high mechanical properties at elevated temperatures. Tjong [1] summarized that, compared to ex-situ composites, the advantages of in-situ composites, which include these formed directly from a liquid, e.g. by the eutectic reaction, are mainly the result from 1) high thermodynamic stability of strengthening phase in the matrix, which allows maintaining high mechanical properties at elevated temperatures, 2) clean reinforcement-matrix interfaces, resulting in strong interfacial bonding and 3) more uniform distribution of the strengthening phase in the matrix.

In the present work the in-situ composites from Fe-Cr-Ni-Mo-C alloy system were synthesized. The major aim of the work was to introduce additional hard phases, besides eutectic carbides, such as intermetallic compounds. In stainless steels precipitation of intermetallic compounds, such as the χ phase and the σ phase, reduces toughness and corrosion resistance [2-6]. Nonetheless, Kim et al. [7] show that hard and brittle FeAl-type intermetallic compound can be effectively used as a strengthening second phase in high-aluminum low-density steel, while decreasing its harmful effect on ductility. This can be achieved by controlling morphology and dispersion of the phase. On the other hand, Suganuma et al. [8] demonstrated that it is possible to improve the ductility of ferritic stainless steels, deformed at elevated temperatures without decreasing the tensile strength. It might be performed by niobium addition, causing a change in the χ phase morphology. Lu et al. [9] showed that the presence of σ phase in a corrosive environment reduces wear rates of ferritic stainless steels. Improvements in the wear resistance of duplex stainless steels associated with the presence of σ phase, were observed, inter alia, by Wang et al. [10] and Fargas et al. [11].

2. Experimental details

2.1. Materials

The chemical compositions of the Fe-Cr-Ni-Mo-C alloys in this study were selected based on thermodynamic calculations. Alloys were synthesized in an arc furnace Arc Melter AM (Edmund Bühler GmbH). Processing was carried out in an argon

* AGH UNIVERSITY OF SCIENCE AND TECHNOLOGY, FACULTY OF METALS ENGINEERING AND INDUSTRIAL COMPUTER SCIENCE, AL. A. MICKIEWICZA 30, 30-059 KRAKOW, POLAND
** AGH UNIVERSITY OF SCIENCE AND TECHNOLOGY, ACADEMIC CENTRE FOR MATERIALS AND NANOTECHNOLOGY, AL. A. MICKIEWICZA 30, 30-059 KRAKOW, POLAND
# Corresponding author: kwiecz@agh.edu.pl

atmosphere using titanium as getter. Mixtures of Fe-C alloy (with known carbon content –4.3 wt.%) with high purity (>99.9%) elements such as chromium, molybdenum, nickel and iron were used as the starting materials. In order to ensure homogeneity of chemical composition, the ingots were re-melted four times. The obtained ingots had a mass of approx. 35 g. The chemical composition of the ingots was analysed on the cross-sections with optical emission spectrometer Foundry-Master (WAS). The results are summarized in Table 1. Subsequently, from a half of each ingot, using a special water-cooled suction casting unit, rods with 5 mm in diameter and length of 55 mm were synthesized (Fig. 1). Thermal control during arc melting is very difficult. Nonetheless Kozieł [12] estimated that the axial cooling rate during solidification for 5 mm cast rod, based on the cellular spacing in the Fe-25Ni (wt.%) alloy, produced in the same unit as in this study, is about 30°C/s. It should be noted that the nickel equivalent (Ni_{eq}) shown in Table 1 is underestimated, because carbon content was not included in the calculation, as carbon is mostly bonded in carbides and its real value in the matrix is difficult to estimate. Simultaneously, the chromium equivalent (Cr_{eq}) might be slightly overestimated, because some part of carbide forming elements such as Cr and Mo are also bonded in carbides. As it can be seen from Table 1, chemical compositions of alloys were selected in order to obtain different Ni_{eq} and Cr_{eq} with similar carbon content and, consequently, to change phase composition of the matrices.

TABLE 1

Chemical compositions of investigated alloys from the Fe-Cr-Ni-Mo-C system (wt. %)

Alloy	C	Cr	Ni	Mo	Si	Mn	P	S	Fe	Cr_{eq}^*	Ni_{eq}^*
1	0.63	24.2	4.2	5.1	0.17	0.11	0.01	0.02	bal.	29.56	4.26
2	0.64	23.8	11.3	4.3	0.18	0.12	0.02	0.02	bal.	28.27	11.36
3	0.67	30.3	11.5	5.5	0.20	0.14	0.03	0.03	bal.	36.10	11.57

* Formulae for calculation [13]:

$Cr_{eq}^* = \%Cr + \%Mo + 1.5 \times \%Si + 0.5 \times \%Nb + 2 \times \%Ti$

$Ni_{eq}^* = \%Ni + 30 \times \%C + 0.5 \times \%Mn$

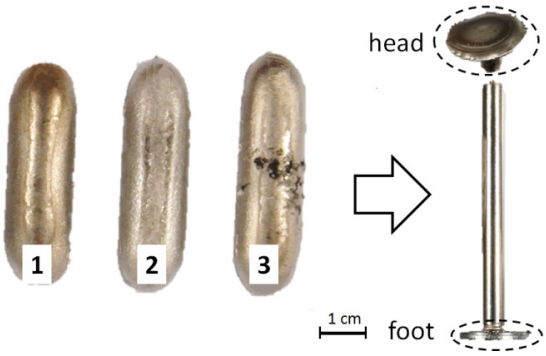

Fig. 1. Synthesized ingots and an example of the suction-cast ϕ 5×55 mm rod

2.2. Thermodynamic simulations

In order to predict phase composition in equilibrium conditions, thermodynamic calculations of selected alloys from the Fe-Cr-Ni-Mo-C system were performed. For this purpose Thermo-Calc software [14] with database for steels/Fe-alloys (TCFE7) was used. The volume fractions of phases vs temperature plots were performed for three model alloys Fe-25Cr-5Ni-5Mo-0.65C, Fe-25Cr-10Ni-5Mo-0.65C and Fe-30Cr-10Ni-5Mo-0.65C. The alloys were selected in order to determine an effect of different chromium and nickel additions on changes in phase composition and their volume fraction, as well as matrix phase transformation temperatures in the investigated system.

2.3. XRD analysis

For X-ray diffraction (XRD) measurement, chips from the suction-cast rod were obtained by turning and subsequent milling to powder using a commercial Mixer Mill MM 400 from Retsch. Milling was carried out in the wet mode using ethanol. Identification of phases after non-equilibrium crystallization was performed by Panalytical Empyrean diffractometer using CoKα1 radiation (λ = 1.7890 Å). The phases were identified using XRD data in the 2θ range from 40 to 100° obtained in the conditions: voltage of 40 kV, current of 40 mA. For the measurements a Göbel Mirror was used.

2.4. Microstructure analysis

The microstructure of the investigated alloys in as-cast state was examined by FEI VERSA 3D scanning electron microscope (SEM), equipped with an energy dispersive spectroscopy (EDS) detector. Investigations were carried out on cross-sections of the ingots after grinding and polishing. To analyse chemical distribution in the observed phases, X-ray mapping was performed. For these measurements accelerating voltage of 15 kV and current of 8 nA were used. Finally, the volume fraction of hard phases (carbides + intermetallic compounds) was estimated by the point counting technique. Additionally, hardness of the alloys was verified by Vickers hardness testing using 1 kgf load (HV1) with a 10 s indentation time. At least five measurements on each sample were performed.

2.5. High-resolution dilatometry

Dilatometric investigations were performed in order to estimate the critical temperatures in the investigated alloys using a high resolution dilatometer Linseis L78 R.I.T.A. Specimens, ϕ 3×10 mm, were turned from the suction-cast rods for these measurements. The specimens were heated with the rate of 0.08°C/s up to partial melting (approx. 1300°C) and subsequently cooled as quickly as possible (at the high temperature range the cooling rate was about 80°C/s). Experiment was performed in a helium atmosphere.

3. Results and discussion

3.1. Thermodynamic simulations

Fig. 2 shows the volume fraction of phases vs temperature plots of three model alloys. As it can be seen in the analysed range of Fe-Cr-Ni-Mo-C system, six phases might occur, i.e. α or δ, γ, $M_{23}C_6$ type carbide, χ phase, σ phase and P phase. The last three are known as topologically closed-packed phases. The black line on the plots corresponds to the sum of hard phases in the alloys, i.e. carbides and intermetallic compounds. In each alloy solidification begins with the appearance of δ crystals. During solidification, alloying elements are shifted to the liquid, which results in the formation of γ phase and eutectic $M_{23}C_6$ carbides. Further cooling at equilibrium conditions causes a slight increase of volume fraction of carbides and precipitation of intermetallic compounds, as well as phase transformations of the matrix. Increase in nickel content in alloy 2, in comparison with alloy 1, changes the range of γ phase stability and significantly affects the formation of intermetallic compounds, promoting precipitation of σ phase in the place of χ and enhancing temperature range of its prevalence. Furthermore, addition of 5 wt.% Ni to alloy 1 restricts the solidification range. Increasing the chromium content in the alloy 3 causes disappearance of χ phase and a clear increase in the volume fraction of σ phase and enhanced temperature stability of carbides.

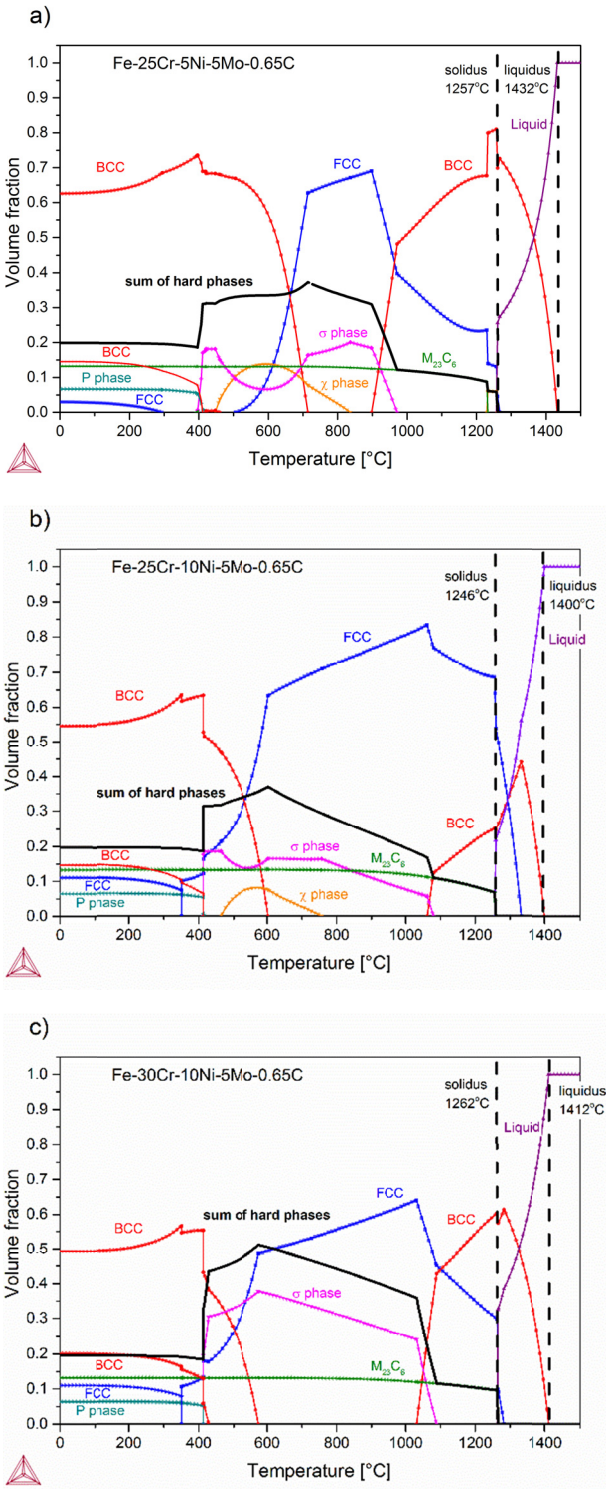

Fig. 2. ThermoCalc calculations for volume fractions of phases vs temperature in model alloys: a) – Fe-25Cr-5Ni-5Mo-0.65C, b) – Fe-25Cr-10Ni-5Mo-0.65C, c) – Fe-30Cr-10Ni-5Mo-0.65C

3.2. X-Ray Diffraction analysis

Fig. 3 shows XRD patterns of the as-cast Fe-Cr-Ni-Mo-C alloys. The Fe-24.2Cr-4.2Ni-5.1Mo-0.63C alloy (alloy 1) includes three phases, i.e. Fe-Cr-Ni-Mo solid solution (α) with BCC crystal structure, $M_{23}C_6$ and M_7C_3 carbides. It is well known that chromium sites in $M_{23}C_6$ and M_7C_3 carbides can be easily replaced by Fe and Mo [15-19], and it can be assumed that these carbides contain the aforementioned, carbide forming elements in their crystal structure. Increase in nickel content in Fe-23.8Cr-11.3Ni-4.3Mo-0.64C alloy (alloy 2) caused significant change in the phase composition (Fig. 3b). The matrix of the alloy, due to nickel being an austenite forming element, exhibits a duplex nature with FCC austenite as the predominant

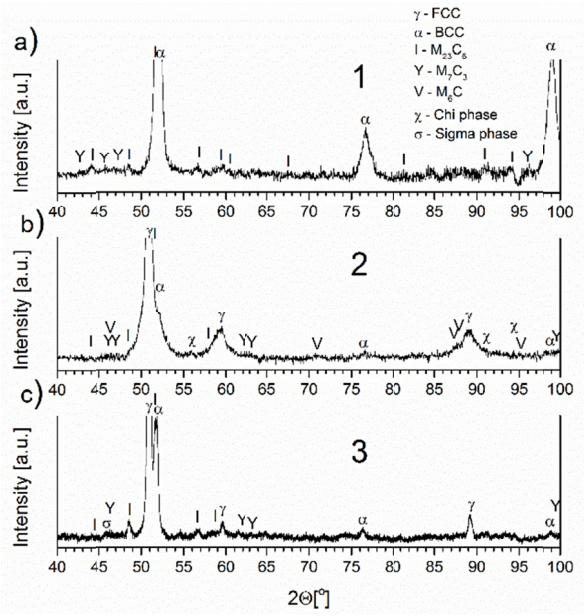

Fig. 3. XRD patterns of the as-cast alloys used in this work: a) – alloy 1, b) – alloy 2, c) – alloy 3

phase. Furthermore, greater nickel content in comparison to alloy 1 resulted in the appearance of additional M_6C carbides and intermetallic compounds such as χ phase. Increase in chromium content in Fe-30.3Cr-11.5Ni-5.5Mo-0.67C alloy (alloy 3) with similar content of other elements in comparison with alloy 2, resulted in the disappearance of M_6C carbides and the appearance of σ phase in place of χ phase (Fig. 3c). Nevertheless, only one peak from (110) σ phase was found at 2Θ equal to 45.71°.

3.3. Microstructure

Fig. 4 shows cross sectional microstructures of alloys used in this work after suction casting (as-cast state). In each alloy a dendritic microstructure, typical for alloys solidified in a high thermal gradient, was observed. BSE imaging allowed us to distinguish easily regions enriched in elements with respect to their atomic number. The atomic numbers of Fe, Cr, Ni and Mo are 26, 24, 28 and 42, respectively. It seems clear that brighter regions observed in the microstructure are enriched in Mo, which strongly segregates to interdendritic regions during solidification. Therefore, the interdendritic zones are preferential sites for carbide nucleation and growth.

In alloy 1 carbides were found only in the interdendritic regions (Figs. 4a and b). These carbides were directly formed from liquid during the eutectic reaction. They exhibit very fine lamellar morphology. Microstructural observations revealed no evidence of secondary carbides. As it can be seen from Fig. 5a,

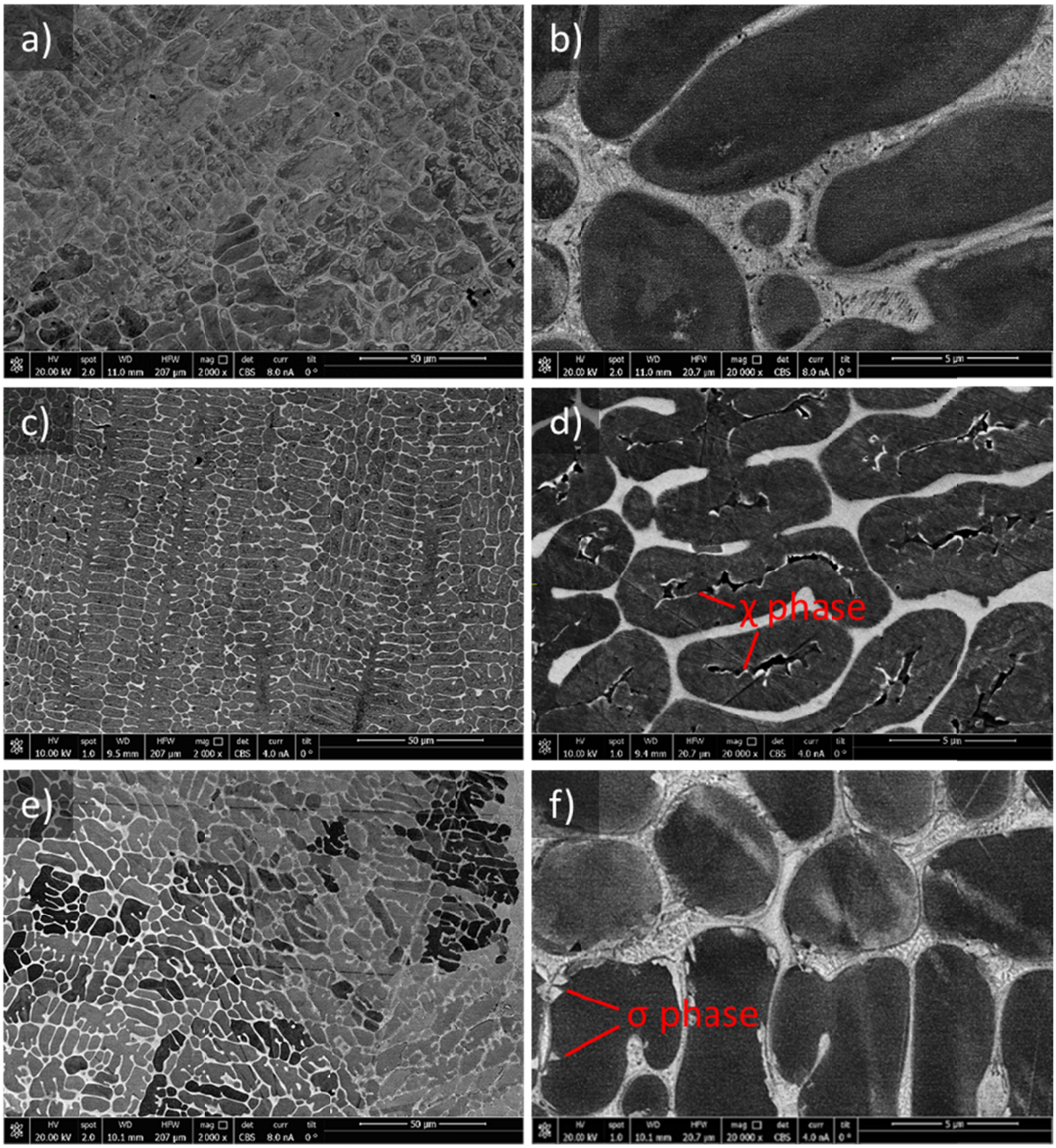

Fig. 4. BSE micrographs of the investigated alloys: a,b) – Fe-24.2Cr-4.2Ni-5.1Mo-0.63C alloy, c,d) – Fe-23.8Cr-11.3Ni-4.3Mo-0.64C alloy, e,f) – Fe-30.3Cr-11.5Ni-5.5Mo-0.67C alloy

the carbides are enriched in Cr and Mo, which is a consequence of strong elemental partitioning during solidification and greater carbon affinity in comparison with Fe. The differences in contrast (brighter and darker regions) in particular dendrites, observed in Figs. 4a, b and 5a, most probably result from casting stresses and some distortion of the matrix crystal lattice.

Figs. 4c and d show a typical microstructure of alloy 2, where six phases where identified (see Fig. 3b) γ solid solution, small amount of α solid solution, 3 types of carbides: M_7C_3, $M_{23}C_6$ and M_6C, and an intermetallic compound – χ phase. The χ phase is located most probably in the centre of dendrites, as indicated in Fig. 4d. Additionally, in the vicinity of χ phase cracks were observed. In the centres of dendrites trace amounts of carbon were found, as shown in Fig. 5b. It is well known that carbon can dissolve in χ phase and stabilize it. Due to this property, the χ phase was defined as $M_{18}C$ type carbide in the past [17,20]. Furthermore, the χ phase is enriched in Cr and Mo in comparison with the matrix [21-23], which explains why it is visible as a bright phase in BSE contrast. The formation of χ phase results from the high supersaturation of first crystals, as a consequence of non-equilibrium solidification with a relatively high cooling rate. The solidification mode in equilibrium of alloy 2 is $L \rightarrow L + \delta \rightarrow L + \delta + \gamma_1 \rightarrow \delta + \gamma_1 + M_{23}C_6$ (see Fig. 3b). This sequence results in the formation of δ/γ interfaces, which are preferential sites for χ phase nucleation [21, 22]. Michalska and Sozańska [22] show that in 2205 duplex steel χ phase precipitates at the ferrite–austenite interface and into the adjacent ferrite matrix. Kinetics of precipitation of intermetallic compounds such as χ, σ or Laves phases strongly depend on chemical composition of the alloy. Campbell [24] reported that in Fe-28Cr alloys, increasing Mo addition from 0 to 5 wt% significantly shifts the temperature-time-precipitation (TTP) curves for χ and σ to shorter times. Furthermore, the results indicate that χ phase precipitates faster than σ. Streicher [25] studied alloys containing 28Cr-4Mo and 28Cr-4Mo-4Ni, and found that nickel additions accelerated σ and χ formation. Cieslak et al. [26] found that χ phase can form in the solid state during high cooling rates, which occur in welds from 316 austenitic steel. Additionally, similar morphology of χ phase as in alloy 2, was reported by Llorca-Isern et al. [27]. During precipitation, the χ phase consumed Cr and Mo, which causes the surrounding areas to be depleted in these elements. It might explain why peaks from austenite and ferrite are considerably wider in comparison with alloys 1 and 3 (see Fig. 3).

The microstructure of alloy 3 is shown in Figs. 4e and f. It was found that eutectic carbides have two morphologies, i.e. complex, very fine lamellar, and those resembling solid carbides. Furthermore, at the carbides/matrix interfaces an additional, most probably σ, phase was found. Unfortunately, its size does not allow us to define the differences in composition in comparison with eutectic carbides (Fig. 5c).

Fig. 6 shows estimated volume fractions of hard phases in the investigated alloys and results of hardness measurements. It should be noted that the χ phase was not included in the calculation of volume fractions of hard phases for alloy 2. As it can been seen from this figure, the volume fractions of hard phases

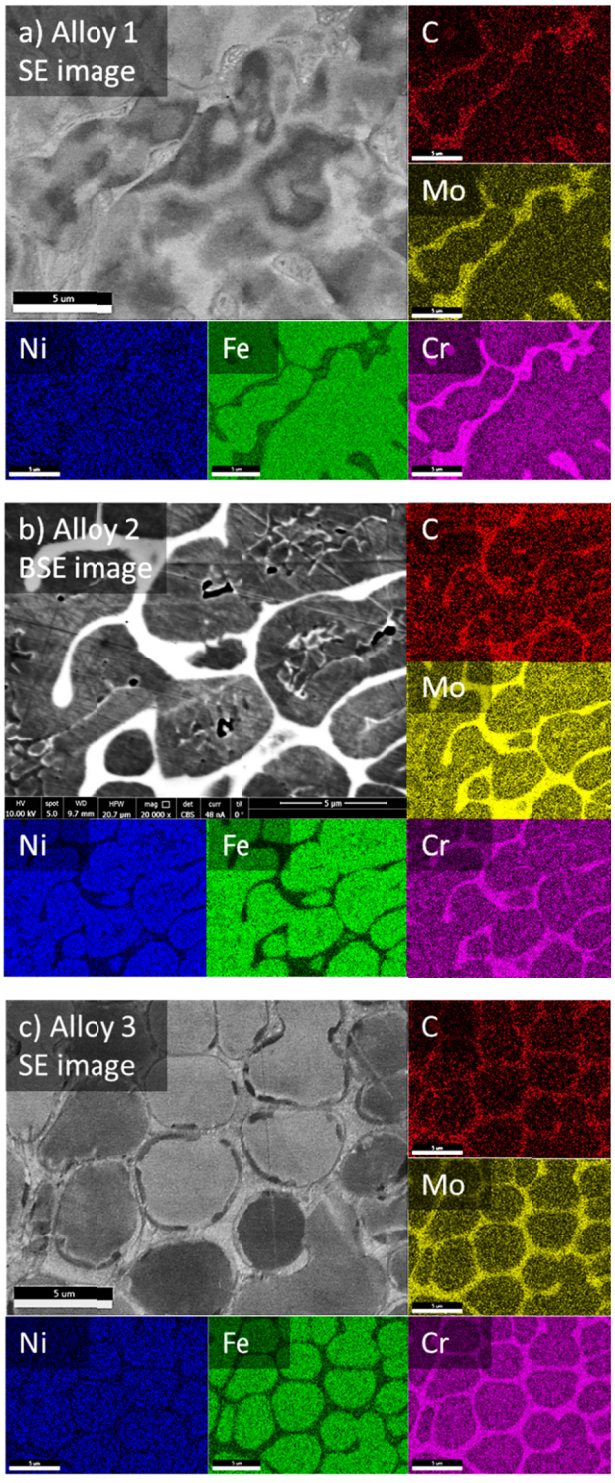

Fig. 5. SEM micrographs and maps of elemental distribution in the investigated alloys: a) – Fe-24.2Cr-4.2Ni-5.1Mo-0.63C alloy, b) – Fe-23.8Cr-11.3Ni-4.3Mo-0.64C alloy, c) – Fe-30.3Cr-11.5Ni-5.5Mo-0.67C alloy

in alloys 1 and 2 are similar and are approx. 18%, while alloy 3 contains a significantly greater amount of hard phases – approx. 30%. The hardness of alloys 1 and 2 are also congruent and are 346 ±4 and 340 ±4 HV1, respectively, despite the fact that matrices in both alloys are significantly different. Additionally, an increase in hardness of alloy 2 is associated with the presence of χ phase, acting as barriers for dislocation motion. Simultane-

ously, a negative effect of cracks in the vicinity of χ phase on hardness cannot be ignored. The average hardness of alloy 3 is 393 ±8 HV1 and results from a high volume fraction of hard phases and solution strengthening.

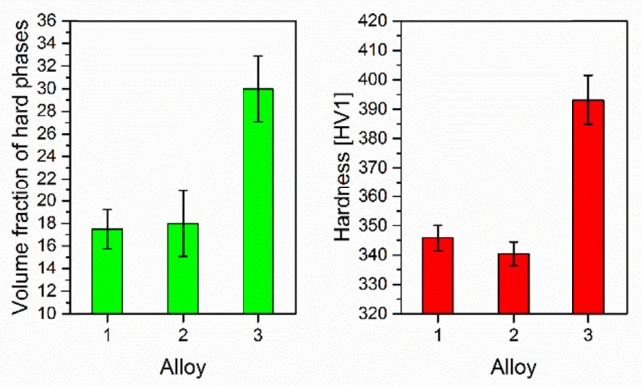

Fig. 6. Volume fractions of hard phases in alloys used in this work and results of hardness measurements

3.4. Dilatometric analysis

Fig. 7 shows changes in the length of dilatometric specimens vs temperature (ΔL) with corresponding differential curves Δ(ΔL)/ΔT and calculated linear thermal expansion coefficient (α_c) of the investigated alloys. The α_c values below 200°C are not shown due to the limitation in the low temperature range of push rod made from Al_2O_3, used in the experiments. The dilatometric effects on the presented curves allow us to determine the temperatures of phase transformations, while the slope gives a rough information about the phase composition of the matrix. With increasing content of austenite in the alloy, the slope of a curve increases. Consequently, a linear thermal expansion coefficient – α_c exhibits greater values. The dilatation negative effects on ΔL curves are the result mainly of the $\alpha \rightarrow \gamma$ phase transformation, but the effects of metastable, non-equilibrium phases dissolution, in-situ transformations (e.g. $M_7C_3 \rightarrow M_{23}C_6$ [28]) and precipitation of intermetallic compounds cannot be excluded. The smallest dilatation effects were observed in alloy 1 with single phase – BCC matrix, while the greatest were found in alloy 2 with a duplex matrix, which is based on Ni_{eq} and Cr_{eq} and contains the largest volume fraction of the FCC phase. The sequence of phase transformations calculated using ThermoCalc seems to be in a good agreement with the experimental results. The differences in the critical temperatures ($\alpha \rightarrow \gamma$, solidus, etc.) might arise from minor variations in the chemical composition of melts and model alloys used in the thermodynamic calculations and non-equilibrium phase composition of synthesized alloys. The wide range of $\alpha \rightarrow \gamma$ transformation temperature and two maxima in alloy 2 are evidence for non-uniform chemical distribution in the α phase. As mentioned above, the χ phase consumed Cr and Mo from the matrix and consequently regions depleted in ferrite formers caused the appearance of the $\alpha \rightarrow \gamma$ transformation maximum at approx. 670°C. These results are in a good agreement with the XRD investigations (section 3.2). In alloy 3 the α_c values are comparable to those of alloy 1. The strong negative dilatation effect between 600 and 760°C resulted from greater amount of FCC phase, formed during $\alpha \rightarrow \gamma$ transformation.

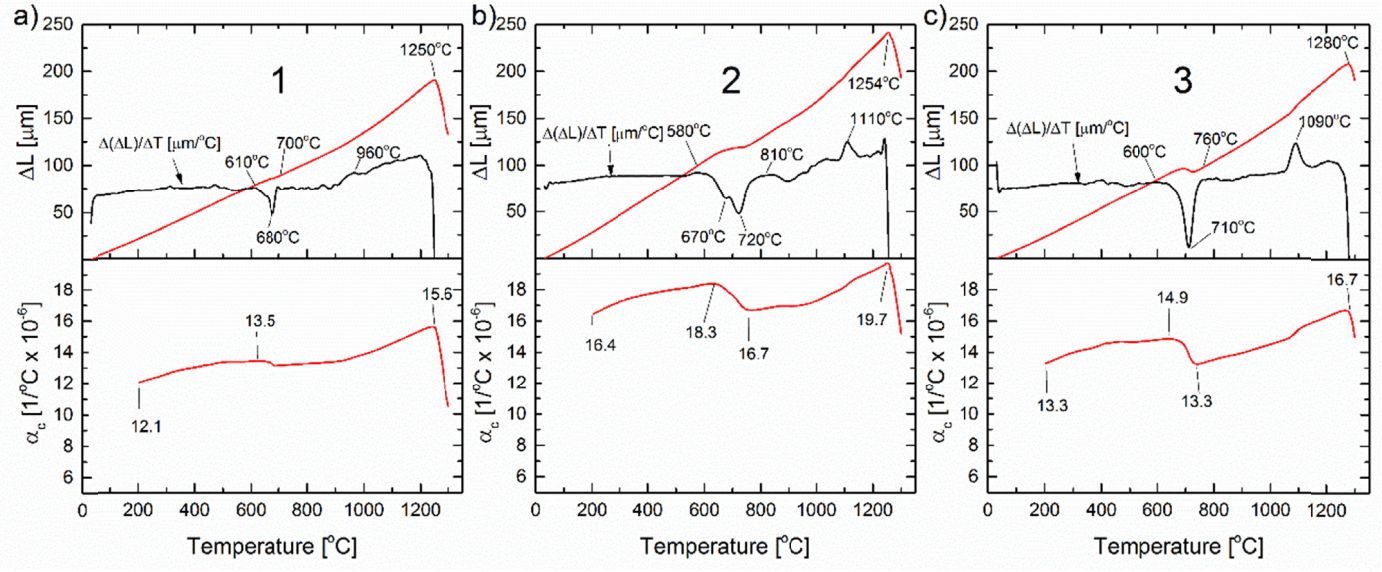

Fig. 7. Dilatograms of heating with the corresponding differential curves Δ(ΔL)/ΔT and calculated linear thermal expansion coefficient – α_c: a) – alloy 1, b) – alloy 2, c) – alloy 3

4. Conclusions

In the present work three alloys from the Fe-Cr-Ni-Mo-C system were synthesized and characterized in the as-cast state. The work showed that by varying the chemical composition of the alloy with respect to Ni_{eq} and Cr_{eq} in complex, in-situ composites, it is possible to introduce intermetallic compounds such as χ or σ. Nonetheless, the place of intermetallic compounds precipitation strongly depends on matrix nature. The phase compositions of the investigated alloys, synthesized in non-equilibrium conditions, significantly differ from calculated, equilibrium phase compositions. Thermodynamic calculations allowed us to predict the sequence of phase transformations in alloys used in this work and they are in a good agreement with the dilatometric investigations.

REFERENCES

[1] S. Tjong, Mater. Sci. Eng. R Reports. **29**, 49-113 (2000).
[2] A.I. Filho, W. da S. Cardoso, L.C. Gontijo, R.V. da Silva, L.C. Casteletti, Metall. Mater. **66**, 467-471 (2013).
[3] J.O. Nilsson, A. Wilson, Mater. Sci. Technol. **9**, 545-554 (1993).
[4] M. Pohl, O. Storz, T. Glogowski, Mater. Charact. 58, 65-71 (2007).
[5] K. Chan, S. Tjong, Materials (Basel). **7**, 5268-5304 (2014).
[6] G. Fargas, M. Anglada, A. Mateo, J. Mater. Process. Technol. **209**, 1770-1782 (2009).
[7] S.-H. Kim, H. Kim, N. J. Kim, Nature. **518**, 77-79 (2015).
[8] K. Suganuma, H. Kayano, S. Yajima, J. Mater. Sci. **16**, 3131-3140 (1981).
[9] X.-C. Lu, S. Li, X. Jiang, Wear. **251**, 1234-1238 (2001).
[10] Y.Q. Wang, J. Han, H.C. Wu, B. Yang, X.T. Wang, Nucl. Eng. Des. **259**, 1-7 (2013).
[11] G. Fargas, A. Mestra, A. Mateo, Wear. **303**, 584-590 (2013).
[12] T. Koziel, Arch. Metall. Mater. **60**, 765-771 (2015).
[13] A.L. Shaeffler, Met. Prog. **56**, 680 (1949).
[14] J.O. Andersson, T. Helander, L. Höglund, P.F. Shi, B. Sundman, Calphad. **26**, 273-312 (2002).
[15] K. Wieczerzak, P. Bala, M. Stepien, G. Cios, T. Koziel, JMADE. **94**, 61-68 (2016).
[16] K. Wieczerzak, P. Bała, M. Stępień, G. Cios, T. Kozieł, Arch. Metall. Mater. **60**, 769-782 (2015).
[17] H.J. Goldschmidt, Interstitial alloys, 1967 Springer Science+Business Media, LLC, New York.
[18] M. Palcut, M. Vach, R. Cicka, J. Janovec, Arch. Metall. Mater. **53**, 1157-1164 (2008).
[19] C.P. Tabrett, I.R. Sare, M.R. Ghomashchi, Int. Mater. Rev. **41**, 59-82 (1996).
[20] B. Weiss, R. Stickler, Metall. Trans. **3**, 851-866 (1972).
[21] D.M. Escriba, E. Materna-Morris, R.L. Plaut, A.F. Padilha, Mater. Charact. **60**, 1214-1219 (2009).
[22] J. Michalska, M. Sozańska, Mater. Charact. **56**, 355-362 (2006).
[23] S.K. Ghosh, S. Mondal, Mater. Charact. **59**, 1776-1783 (2008). doi:10.1016/j.matchar.2008.04.008.
[24] R.D. Campbell, Key Eng. Mater. **69-70**, 167-216 (1992).
[25] M.A. Streicher, Corrosion. **30**, 115-124 (1974).
[26] M.J. Cieslak, A.M. Ritter, W.F. Savage, Weld. J. **63**, 133-140 (1984).
[27] N. Llorca-Isern, H. López-Luque, I. López-Jiménez, M.V. Biezma, Mater. Charact. **112**, 20-29 (2016).
[28] A. Inoue, T. Masumoto, Metall. Trans. **A. 11**, 739-747 (1980).